Available online at www.sciencedirect.com
SCIENCE DIRECT®
International Journal of Heat and Fluid Flow 26 (2005) 92–104
International Journal of HEAT AND FLUID FLOW
www.elsevier.com/locate/ijhff

Evaluating the role of subgrid stress modeling in a ribbed duct for the internal cooling of turbine blades

D.K. Tafti *

Mechanical Engineering Department, Virginia Tech, 105 Randolph Hall, Blacksburg, VA 24061, USA

Received 8 January 2004; accepted 5 July 2004
Available online 27 August 2004

Abstract

Time-dependent simulations are performed in a ribbed square duct with rib height to hydraulic diameter ratio of 0.1 and rib pitch to rib height ratio of 10. The calculations are performed for a nominal bulk Reynolds number of 20,000. Hydrodynamic and thermal fully-developed conditions are assumed. Two mesh resolutions, 96^3 and 128^3 are tested in a quasi-DNS mode and in LES mode with the Dynamic Smagorinsky model. Time evolution, mean, and turbulent quantities are presented, together with friction and heat transfer. It is found that in general, both quasi-DNS and LES resolve the bulk mean features of the flow within 10–15% of each other. These include recirculation patterns and secondary flows which are characteristic of this geometry. However, there are large differences in predicting the friction and heat transfer coefficients, both of which are very sensitive to the predicted turbulent field near the duct surfaces. Both quasi-DNS calculations underpredict the heat transfer and friction coefficient by amounts which range between 20% and 30% on the 96^3 mesh and 15–20% on the 128^3 mesh. However, the LES calculations with the dynamic Smagorinsky model predict these quantities within 5–10% of experimental values for both mesh resolutions. It is concluded that in an average sense, the level of turbulence augmentation provided by the dynamic model is commensurate with the mesh resolution such that the turbulent energy, heat transfer coefficient, and friction are predicted at the right levels independent of the resolution.

Keywords: LES; Dynamic Smagorinsky model; Ribbed-ducts; Turbine blade internal cooling

1. Introduction

For compact high efficiency turbines to operate at near stoichiometric inlet temperatures, the cooling of turbine blades is a critical issue. Both internal convective cooling and external film cooling are employed for this purpose. Internal passages can take varying cross-sectional shapes depending on their location in the blade. For the most part these passages can be approximated by rectangular or trapezoidal cross-sections. Cooling air from the base of the blade flows through a multi-pass duct or serpentine passage, the surface of which is roughened with turbulence promoters to enhance heat transfer. Turbulence promoters can take varying shapes, sizes, and configurations, ranging from ribs to pin fins, the former being more commonly used.

Over the past two decades numerous experimental studies have investigated the heat transfer characteristics in rib roughened passages. Han and group at Texas A&M (Han, 1984; Chandra et al., 1988; Han, 1988; Lau et al., 1991a; Lau et al., 1991b; Han and Zhang, 1991; Han et al., 1992; Zhang et al., 1995; Ekkad and Han, 1997) have studied the effect of different rib angles (90, ±60, ±45), different rib sections (square, triangular, hemisphere), different rib orientations (parallel on opposing walls, criss-cross), full and discrete ribs, different rib height/hydraulic diameter ratios ($e/D_h = 0.0625 - 0.13$), different rib pitch/height ratios ($P/e = 8 - 30$), different

* Tel.: +1 540 231 9975; fax: +1 540 231 9100.
E-mail address: dtafti@vt.edu

0142-727X/$ - see front matter © 2004 Elsevier Inc. All rights reserved.
doi:10.1016/j.ijheatfluidflow.2004.07.002

Nomenclature

C_p	specific heat
D_h	hydraulic diameter, characteristic length
e	rib height
$\vec{e}_x$	unit vector in streamwise or x-direction
f	Fanning friction factor
k	thermal conductivity (W/mK)
L_x	length of domain in x-direction
$\vec{n}$	surface normal vector
Nu	local Nusselt number (Eq. (13))
$\langle Nu \rangle$	spatially averaged Nusselt number (Eq. (15))
P	total pressure OR rib pitch
p	fluctuating, modified or homogenized pressure
Pr	Prandtl number ($=\mu C_p/k$)
q''	constant heat flux boundary condition on duct walls and rib. ($q'' D_h/k$) is characteristic temperature scale
Q_x	Flow rate in x-direction
Re_b	Reynolds number ($=\bar{u}_b D_h/\nu$)
Re_τ	Reynolds number ($=u_\tau D_h/\nu$)
Re_{t_τ}	turbulent Reynolds number ($=u_\tau D_h/\nu_t$)
T	temperature
$\vec{u}$	Cartesian velocity vector (u,v,w) or (u_1,u_2,u_3)
$\bar{u}_b$	mean bulk flow velocity, characteristic velocity used for non-dimensionalizing results
u_τ	friction velocity, characteristic velocity used in computations
$\vec{x}$	physical coordinates (x,y,z) or (x_1,x_2,x_3)
x'	measured from downstream edge of rib
β	mean pressure gradient
γ	mean temperature gradient
θ	fluctuating, modified or homogenized temperature
Ω	total heat transfer surface area
$\vec{\xi}$	computational coordinates (ξ,η,ζ)

Subscripts

s	surface
b	mean time averaged velocity, also used for average bulk velocity
0	smooth duct
rms	root mean square
x	in streamwise direction

aspect ratio channels ($H/W = 1/4 - 4$), and variable temperature and flux boundary conditions in a Reynolds number range from 10,000 to 100,000. Taslim and group (Korotky and Taslim, 1998; Taslim et al., 1998; Taslim and Lengknong, 1998; Taslim and Korotky, 1998) have also performed similar studies.

From these and others the following general conclusions are reached:

- Roughness elements enhance the heat transfer coefficient by a factor of 2–4 over smooth surfaces on the ribbed walls (usually leading and trailing surfaces of blade) and an additional enhancement between 1.5 and 2 on the non-ribbed surfaces or side walls.
- Optimal heat transfer enhancement is provided by ribs angled at 45–60° to the flow direction with $e/D_h \approx 0.1$ and $P/e \approx 10$.

Prediction of these flows has been complicated by the presence of separating/reattaching shear layers, secondary flows induced by 90° bends, rotational Coriolis, and centrifugal buoyancy forces. The turbulent flow is anisotropic and most attempts at predicting the flow and heat transfer have focused on the solution of steady Reynolds–averaged Navier–Stokes (RANS) and energy equations. Different closure models have been used with varying degrees of success. Eddy-viscosity type models (Prakash and Zerkle, 1992; Prakash and Zerkle, 1995), which assume isotropy do not perform very well, while more complicated models based on the solution of the turbulent stress equations (Jang et al., 2001; Han et al., 2002; Jia et al., 2002) have been found to perform reasonably well.

Our objective is to evaluate and develop techniques based on the time-accurate resolution of these flows. In this class of methods, the technique which is the subject of this paper is large-eddy simulation (LES). By resolving only the energy containing eddies, LES reduces the computational complexity of direct numerical simulations (DNS) by several orders of magnitude. To perform LES, one could follow two approaches, both of which have seen varied use. In the most commonly used approach, explicit subgrid stress models are used to model the unresolved subgrid stresses. Another approach is the use of monotonic integrated large-eddy simulations (MILES).

A number of subgrid-scale models varying in complexity from eddy-viscosity to one equation models exist. Recent reviews can be found in Ferziger (1996) and Lesieur and Metais (1996). The most widely used closure model, suggested by Smagorinksy (1963), is based on Boussinesq's approximation in which the subgrid-scale Reynolds stresses are related to the strain rate tensor of the resolved field through an eddy viscosity. The eddy viscosity is computed from the resolved strain rate magnitude and a characteristic length scale. The length scale is assumed to be proportional to the filter width *via* a Smagorinsky constant. To address the shortcomings of the Smagorinsky model in transitional and wall bounded flows, Germano et al. (1991) proposed a

dynamic procedure for the computation of the Smagorinsky constant. The constant is dynamically calculated based on the local characteristics of turbulence and hence provides flexibility and preempts any ad hoc tuning of the model constant.

An alternative to the use of explicit subgrid-scale models for LES is the use of monotonic integrated large-eddy simulations (MILES) (Boris et al., 1992). These encompass a general class of methods which maintain the monotonicity (do not give rise to spurious oscillations) of the integrated field (also referred to as shock capturing schemes, total variation diminishing (TVD), essentially non-oscillatory, positivity preserving, shape preserving). They differ in detail but are designed to support the minimal diffusion that is required to preserve the shape of a distribution during transport. In this class, the FCT method (Boris and Book, 1973) has been used successfully by Fureby and Grinstein (2000) for free shear layers as well as high Reynolds number wall bounded flows.

In internal cooling geometries Murata and Mochizuki (2001, 2000) have performed LES for low Reynolds number flows ($Re_b < 10{,}000$) in ribbed channels with Coriolis and buoyancy effects. They used the Lagrangian dynamic subgrid stress model (Meneveau et al., 1996). Recently, Watanabe and Takahashi (2002) have simulated a Reynolds number of 1.17×10^5 with a resolution of $104 \times 78 \times 75$ using both the Smagorinsky and dynamic Smagorinsky models. They showed good agreement with experimental results.

Our objective in this paper is to evaluate the role of subgrid scale modeling for demanding high Reynolds number heat transfer applications encountered in internal cooling flows and to shed light on their contribution, accuracy and suitability. An additional objective is to elucidate on the physics pertaining to the hydrodynamics, in particular the role of turbulence in augmenting heat transfer. Here we present results from four calculations performed with a second-order central differencing scheme in a quasi-DNS mode and an LES mode with the dynamic Smagorinsky model (DSM). Two mesh resolutions, $128 \times 128 \times 128$ and $96 \times 96 \times 96$ are evaluated for a nominal bulk Reynolds number of 20,000 in a square channel with normal ribs with $e/D_h = 0.1$ and $P/e = 10$. In the rest of the paper, the quasi-DNS calculations are referred to by the mesh size (e.g. 96^3), and for the LES calculations the mesh size appended with DSM is used (e.g. 128^3-DSM).

1.1. Computational model and governing equations

The computational model assumes fully-developed flow and heat transfer and simulates a periodically repeating spatial unit consisting of two ribs (one on either side of the duct) as shown in Fig. 1(a). The duct walls as well as all six faces of the two ribs exposed to the main flow are heated by imposing a constant heat flux (q'') boundary condition. The governing flow and energy equations are non-dimensionalized by a characteristic length scale which is chosen to be the hydraulic diameter of the channel (D_h), a characteristic velocity scale given by the friction velocity $u_\tau = \sqrt{\Delta \bar{P}_x/\rho}$, and a characteristic temperature scale given by $q'' D_h/k$. The assumed periodicity of the domain in the streamwise or x-direction requires that the mean gradients of pressure and temperature be isolated from the fluctuating periodic components as follows:

$$\begin{aligned} P(\vec{x},t) &= P_{in} - \beta x + p(\vec{x},t), \\ T(\vec{x},t) &= T_{in} + \gamma x + \theta(\vec{x},t), \end{aligned} \tag{1}$$

where β is the mean pressure gradient, p is the fluctuating pressure, γ is the mean temperature gradient, and θ, the fluctuating temperature.

On substitution into the Navier–Stokes and energy equations, the *non-dimensional* time-dependent equations in transformed coordinates $\vec{\xi} = \vec{\xi}(\vec{x})$ take the following conservative form: [1]

Continuity:

$$\frac{\partial}{\partial \xi_j}(\sqrt{g}\overline{U}^j) = 0. \tag{2}$$

Momentum:

$$\begin{aligned} &\frac{\partial}{\partial t}(\sqrt{g}\bar{u}_i) + \frac{\partial}{\partial \xi_j}(\sqrt{g}\overline{U}^j \bar{u}_i) \\ &\quad = -\frac{\partial}{\partial \xi_j}(\sqrt{g}(\vec{a}^j)_i \bar{p}) + \frac{\partial}{\partial \xi_j}\left(\left(\frac{1}{Re_\tau} + \frac{1}{Re_{t_\tau}}\right)\sqrt{g} g^{jk} \frac{\partial \bar{u}_i}{\partial \xi_k}\right) \\ &\qquad + \sqrt{g}\beta\delta_{i1}. \end{aligned} \tag{3}$$

Energy:

$$\begin{aligned} &\frac{\partial}{\partial t}(\sqrt{g}\bar{\theta}) + \frac{\partial}{\partial \xi_j}(\sqrt{g}\overline{U}^j \bar{\theta}) \\ &\quad = \frac{\partial}{\partial \xi_j}\left(\left(\frac{1}{PrRe_\tau} + \frac{1}{Pr_t Re_{t_\tau}}\right)\sqrt{g} g^{jk} \frac{\partial \bar{\theta}}{\partial \xi_k}\right) - \sqrt{g}\gamma\bar{u}_1, \end{aligned} \tag{4}$$

where $\vec{a}^i$ are the contravariant basis vectors, [2] $\sqrt{g}$ is the Jacobian of the transformation, g^{ij} are the elements of the contravariant metric tensor, $\sqrt{g}U^j = \sqrt{g}(\vec{a}^j)_k u_k$ is the contravariant flux vector, u_i is the Cartesian velocity vector, and θ is the modified temperature. Here, the overbar denotes grid filtered quantities ($\overline{G}$). Re_{t_τ}, the inverse of the non-dimensional eddy-viscosity is modeled as

$$\frac{1}{Re_{t_\tau}} = C_s^2 (\sqrt{g})^{2/3} \, |\overline{S}|, \tag{5}$$

[1] Henceforth, all usage is in terms of non-dimensionalized values.

[2] The notation $(\vec{a}^j)_k$ is used to denote the kth component of vector $\vec{a}^j \cdot (\vec{a}^j)_k = \partial \xi_j / \partial x_k$.

where $|\overline{S}|$ is the magnitude of the strain rate tensor given by $|\overline{S}| = \sqrt{2\overline{S_{ik}}\,\overline{S_{ik}}}$.

The strain rate tensor is given by

$$\overline{S}_{ik} = \frac{1}{2}\left((\vec{a}^m)_k \frac{\partial \overline{u_i}}{\partial \xi_m} + (\vec{a}^m)_i \frac{\partial \overline{u_k}}{\partial \xi_m}\right) \tag{6}$$

and the Smagorinsky constant C_s^2 is obtained via the dynamic subgrid stress model (Germano et al., 1991). To this end, a second test filter, denoted by $\widehat{G}$, is applied to the filtered governing equations with the characteristic length scale of $\widehat{G}$ being larger than that of the grid filter, $\overline{G}$. The test filtered quantity is obtained from the grid filtered quantity by a second-order trapezoidal filter which is given by $\hat{\phi} = \frac{1}{4}(\bar{\phi}_{i-1} + 2\bar{\phi}_i + \bar{\phi}_{i+1})$ in one dimension. The resolved turbulent stresses, representing the energy scales between the test and the grid filters, $L_{ij} = \widehat{\overline{u_i}\overline{u_j}} - \hat{\bar{u}}_i\hat{\bar{u}}_j$, are then related to the subtest, $T_{ij} = \widehat{\overline{u_i}\overline{u_j}} - \hat{\bar{u}}_i\hat{\bar{u}}_j$, and subgrid-scale stresses $\tau_{ij} = \overline{u_iu_j} - \bar{u}_i\bar{u}_j$ through the identity $L_{ij} = T_{ij} - \hat{\tau}_{ij}$.

The anisotropic subgrid and subtest-scale stresses are then formulated in terms of the Smagorinsky eddy viscosity model as:

$$\hat{\tau}^a_{ij} = -2C_s^2(\sqrt{g})^{2/3}\widehat{|\overline{S}|\,\overline{S}_{ij}}, \tag{7}$$

$$T^a_{ij} = -2C_s^2\alpha(\sqrt{g})^{2/3}\,\hat{|\overline{S}|}\,\hat{\overline{S}}_{ij}. \tag{8}$$

Using the identity

$$\begin{aligned} L^a_{ij} &= L_{ij} - \frac{1}{3}\delta_{ij}L_{kk} = -2C_s^2(\sqrt{g})^{2/3}(\alpha\,\hat{|\overline{S}|}\,\hat{\overline{S}}_{ij} - \widehat{|\overline{S}|\,\overline{S}_{ij}}) \\ &= -2C_s^2(\sqrt{g})^{2/3}M_{ij}. \end{aligned} \tag{9}$$

Here α is the square of the ratio of the characteristic length scale associated with the test filter to that of the grid filter and is taken to be $\lfloor \hat{\Delta}_i/\Delta_i = \sqrt{6} \rfloor$ for a three-dimensional test filtering operation (Najjar and Tafti, 1996). Using a least-squares minimization procedure of Lilly (1992) a final expression for C_s^2 is obtained as:

$$C_s^2 = -\frac{1}{2}\frac{1}{(\sqrt{g})^{2/3}}\frac{L^a_{ij}\cdot M_{ij}}{M_{ij}\cdot M_{ij}}, \tag{10}$$

where the local value of C_s^2 is constrained to positive values. The turbulent Prandtl number is assumed to have a constant value of 0.5 (Moin et al., 1991).

The mean non-dimensional pressure gradient β is assumed to be unity, whereas γ is calculated from a global energy balance as: $\gamma = q''\Omega/Re_\tau Pr\,Q_xL_x$. The boundary conditions imposed on the duct walls and the ribs are as follows:

$$\begin{aligned} &\vec{u} = 0, \\ &\nabla p\cdot\vec{n} = 0, \\ &\nabla\theta\cdot\vec{n} = 1 - \gamma\vec{e}_x\cdot\vec{n} \end{aligned} \tag{11}$$

and in the streamwise direction as:

$$\phi(x + L_x) = \phi(x), \quad \phi = \vec{u}, p, \text{ and } \theta. \tag{12}$$

The governing equations for momentum and energy are discretized with a conservative finite-volume formulation using a second-order central difference scheme on a non-staggered grid topology. The Cartesian velocities, pressure, and temperature are calculated and stored at the cell center, whereas contravariant fluxes are stored and calculated at the cell faces. For the time integration of the discretized continuity and momentum equations, a projection method is used. The temporal advancement is performed in two steps, a predictor step, which calculates an intermediate velocity field, and a corrector step, which calculates the updated velocity at the new time step by satisfying discrete continuity. The energy equation is advanced in time by the predictor step. The computer program Generalized Incompressible Directand Large-Eddy Simulations of Turbulence (GenIDLEST) used for these simulations has been applied extensively to study air-side heat transfer augmentation in compact heat exchangers and other varied applications. Details about the algorithm, functionality, and capabilities can be found in Tafti (2001).

2. Computational details

In this paper we present four calculations with meshes sized at 96^3 and 128^3 computational cells. Table 1 summarizes the calculations, two on each mesh, with and without the dynamic Smagorinsky model (DSM). The mesh distribution for the two resolutions is shown in Fig. 1(b). Mesh density is high in the vicinity of the rib and the duct surface to resolve the turbulent boundary/shear layers, which is crucial to the accurate prediction of turbulence and heat transfer. The mesh distribution in the vicinity of walls strives to keep the first mesh point within $\Delta^+_\perp < 1$ with 4–5 mesh points within 10 wall units. In the present calculations, a posteriori evaluation of the mesh in wall units based on local friction shows that $\Delta^+_\perp \ll 1.0$ over the majority of the duct and rib surfaces ($\Delta^+_{\perp\max} \approx 3$), with streamwise $\Delta^+_{/\!/_1}$, and spanwise $\Delta^+_{/\!/_2}$ varying between 5 and 30 wall units for both mesh resolutions. [3] In addition, the frequency power spectra plotted in Fig. 1(c) at different locations in the computational domain indicate that the resolved grid scales are well beyond the inertial subrange.

The non-dimensional time step in both calculations is set to 5×10^{-5}. The viscous terms are treated implicitly in all cases except for the 96^3 calculation. In all calculations, the average L_1 residual norm of global mass

[3] Although a very good indication of mesh adequacy, it is not sufficient because a coarse mesh will give low values of wall shear stress and hence erroneous low values in wall coordinates.

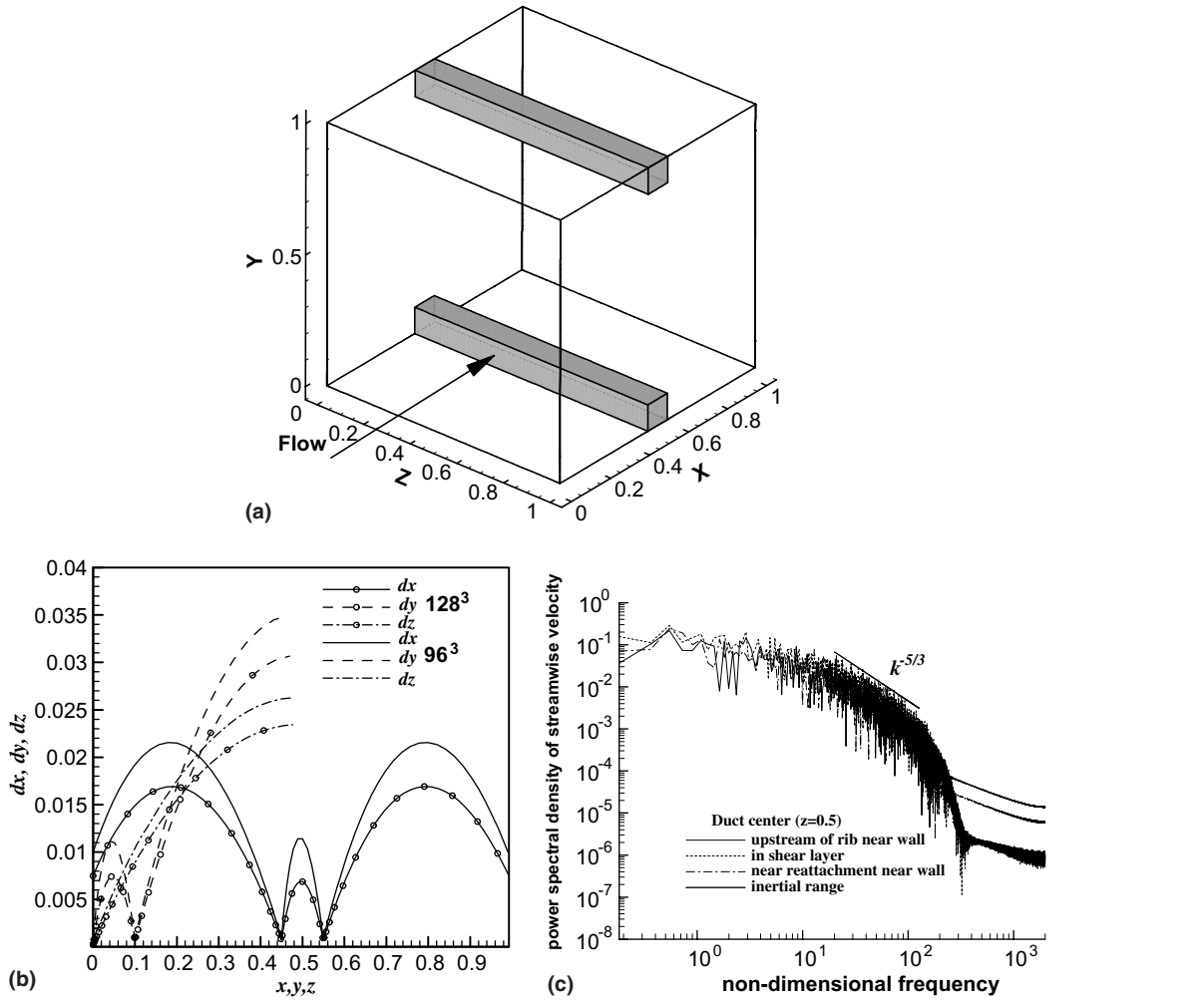

Fig. 1. (a) Computational domain non-dimensionalized by hydraulic diameter. Flow is from left to right. (b) Variation of grid spacing for the two mesh resolutions. The mesh density is largest in the vicinity of the duct walls and the rib. (c) Power spectrum of streamwise velocity at different locations. Resolved grid scales are well beyond the inertial subrange.

balance is converged to 1×10^{-8}, while the momentum and energy equations in the implicit treatment are converged to 1×10^{-7}. All calculations utilize 32 processors of an IA-64 Itanium Linux cluster. Each time step consumes between 30 and 50 μs/grid node of total CPU time or 1–1.5 μs/grid node of wall clock time. Hence, for integrating over one non-dimensional time unit, about 10 and 20 wall clock hours are utilized for the coarse and fine grid, respectively.

Calculations are initiated by assuming an initial flow rate or bulk velocity and integrated in time until the flow rate adjusts to the balance between internal losses and the specified mean pressure gradient. The time evolution of various bulk quantities like form drag losses, friction drag losses, and Nusselt numbers are monitored to ascertain that the flow has reached a statistically stationary state. Once stationary conditions are established, data sampling is initiated to obtain mean and turbulent quantities. Sampling intervals vary from approximately 5 time units for the 128^3 calculation to about 10 time units on the coarse grid. Initial mean quantities of velocities are obtained by sampling over 1 time unit before beginning to sample fluctuating quantities for turbulent statistics. The final statistical sample size is quadrupled by using the bi-directional y–z symmetry of the duct and presenting averaged and turbulent quantities for 1/4th of the duct cross-section.

To facilitate comparison with previous experimental work all the results are normalized by the mean bulk flow velocity $\bar{u}_b$. The local Nusselt number is calculated as:

$$Nu = \frac{1}{\theta_s - \theta_{ref}}, \tag{13}$$

where θ_s is the surface temperature and θ_{ref} is the reference temperature defined as: [4]

[4] For time-averaged Nusslet number θ_s and θ_{ref} are calculated from the time averaged temperature field.

Table 1
Summary of heat transfer and friction data and percentage error with data of Rau et al. (1998)

	Computations, $e/D_h = 0.1$, $P/e = 10$				Rau et al. (1998), $e/D_h = 0.1$, $P/e = 10$
	96^3	96^3 DSM	128^3	128^3 DSM	
Re_τ	6667	6667	6667	6667	–
Re_b	24,000	20,000	22,000	20,000	30,000
% form loss	92	94	92	91	85
Reattachment length (x_r/e)	4.8	4.3	4.6	4.1	4.0–4.25
	$\langle Nu\rangle/Nu_0$ ($Nu_0 = 0.023 \cdot Re_b^{0.8} \cdot Pr^{0.4}$)				
Rib	2.22	2.84	2.54	2.89	–
Ribbed wall	1.78 (−26%)	2.35 (0%)	2.00 (−17%)	2.4 (0%)	2.40
Smooth wall	1.40 (−32%)	1.89 (−7%)	1.60 (−22%)	1.89 (−7%)	2.05
Overall with rib	1.67	2.22	1.89	2.23	–
Overall w/o rib	1.58 (−28%)	2.11 (−4.5%)	1.79 (−19%)	(2.14) (−3.4%)	2.21
	f/f_0 ($f_0 = 0.046 \cdot Re_b^{-0.2}$)				
Overall	6.11 (−36%)	8.53 (−10%)	7.23 (−24%)	8.6 (−9%)	9.5

Experimental uncertainty is ±5%.

$$\theta_{\text{ref}} = \frac{\int\int |u_1|\,\theta\,\mathrm{d}A_x}{\int\int |u_1|\,\mathrm{d}A_x}. \tag{14}$$

The surface-averaged Nusselt number is obtained by averaging the local Nusselt number as:

$$\langle Nu\rangle = \frac{1}{\int\int_\Omega \mathrm{d}S}\left[\int\int_\Omega \frac{1}{\theta_s - \theta_{\text{ref}}}\mathrm{d}S\right], \tag{15}$$

where s denotes the surface under consideration.

Based on the non-dimensionalize mean pressure gradient of unity, the Fanning friction factor is calculated as:

$$f = \frac{1}{2\cdot \bar{u}_b^2}. \tag{16}$$

To calculate the augmentation ratio, reference values for Nusselt number and friction factor for a smooth duct are obtained from the Dittus–Boelter and Blasius correlation, respectively (Incropera and Dewitt, 2002).

$$Nu_0 = 0.023 \cdot Re_b^{0.8} \cdot Pr^{0.4} \tag{17}$$

and

$$f_0 = 0.046 \cdot Re_b^{-0.2}. \tag{18}$$

The computational results are compared with the hydrodynamic and heat transfer data of Rau et al. (1998). Their results for a bulk Reynolds number of 30,000 in a 2-sided ribbed duct with $P/e = 9$ and 10 and $e/D_h = 0.1$ are used for comparison. All mean and turbulent quantities are normalized by the calculated bulk mean velocity, $\bar{u}_b$.

3. Results and discussion

All calculations are performed at $Re_\tau = 6667$ with a mean pressure gradient of unity applied in the flow direction. As the flow develops, the mass flow adjusts such that the losses in the duct are balanced by the applied pressure gradient. Table 1 lists the calculated Re_b for the four calculations. The 96^3 calculation returns the largest value of $Re_b = 24{,}000$, followed by the 128^3 calculation, which predicts $Re_b = 22{,}000$. Both DSM calculations calculate values of 20,000. Higher values of Re_b indicate that predicted losses in the duct are lower. Since frictional losses in the duct are quite dependent on the level of turbulence, it can immediately be concluded from the results in Table 1, that the 96^3 calculation has the lowest turbulence levels. Introduction of DSM increases these levels, increases losses, and lowers the bulk Reynolds number. Although this observation by itself does not lead to any conclusions about the accuracy of the simulations with DSM, it, together with other evidence presented in this paper, does lead to the conclusion that the inclusion of subgrid scale stress modeling results in improved prediction capability.

Fig. 2(a) shows the time evolution of the streamwise component of shear forces integrated over the rib, smooth walls, and the ribbed walls, together with the form drag experienced by the rib. The form drag is obtained by calculating the integrated pressure force differential between the leading and trailing edge of the rib. The plotted quantities are a fraction of the total loss in the streamwise direction (which is unity in the mean). The initial large excursions in calculated quantities are a result of the initial uniform velocity field. [5] The integrated shear forces on the ribbed walls are directed in the negative x-direction as a result of the large recirculation region behind the rib. Similarly, the recirculation region on the top of the rib induces a negative integrated

[5] It is important to have a good guess of the initial bulk flow velocity to avoid excessive integration times to reach a stationary state.

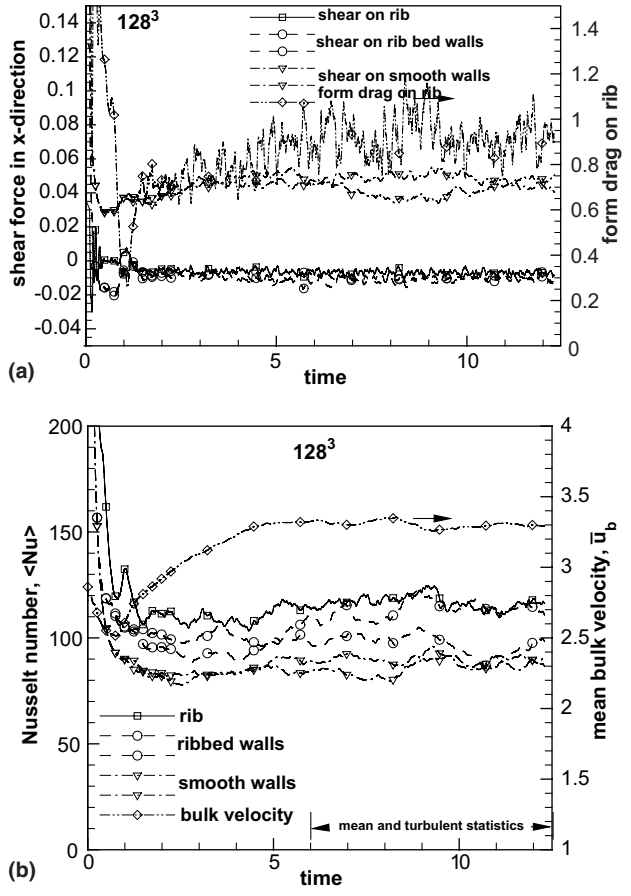

Fig. 2. (a) Evolution of shear forces and form drag on duct surfaces and the rib. The form drag contributes 92% to the overall losses. The negative shear force on the ribbed wall is a result of the recirculation zone. Smooth walls contribute about 9% to total losses. (b) Evolution of surface-averaged Nusselt number and bulk flow velocity with integration time. Spatially averaged Nusselt numbers on component surfaces are presented.

shear force. On the other hand, the smooth walls collectively make a 9–10% mean contribution to the total losses. High shear stresses are concentrated in the region where the ribs meet the side walls. The integrated losses due to form drag show large temporal fluctuations and in the mean contribute about 91% to the total losses. The value compares reasonably well with 85% reported by Rau et al. (1998), who approximated the form drag as a two-point pressure differential at the center line of the ribbed wall, 0.5*e* upstream and downstream of the rib. Table 1 summarizes the mean percentage contribution of form drag (the rest comes from shear losses), which vary between 91% and 94% for the four calculations.

Fig. 2(b) shows the corresponding evolution of the spatially averaged Nusselt numbers ($\langle Nu \rangle$) on the ribbed and smooth walls, and also on the rib. Also shown is the temporal evolution of the bulk mean velocity in the domain. After the initial transient, which lasts for approximately two time units, the Nusselt numbers settle down to a stationary state. However, the bulk flow rate takes longer to adjust and reaches a quasi-steady value at five time units.

Fig. 3(a) shows the mean streamline pattern at the center of the duct ($z = 0.5$) for the 128^3-DSM calculation. The flow is nominally two-dimensional in the symmetry plane. All calculations reproduce the leading edge eddy at the rib–wall junction, the counter-rotating eddy in the rib wake, the main recirculation region and the recirculation region on top of the rib. The prediction of the reattachment length behind the rib is sensitive to the level of turbulence in the separated shear layer and is overpredicted when turbulence is underpredicted. Table 1 compares the predicted reattachment lengths with the experiments of Rau et al. (1998). There is a clear trend towards better prediction accuracy when DSM is included in the calculation. The reattachment length is overpredicted by the 96^3 calculation by approximately 10–15%. However, with the inclusion of DSM, the predicted values are in much better agreement with experiments for both mesh resolutions.

In the vicinity of the smooth walls ($z = 0.0$) the flow field becomes strongly three-dimensional with mean

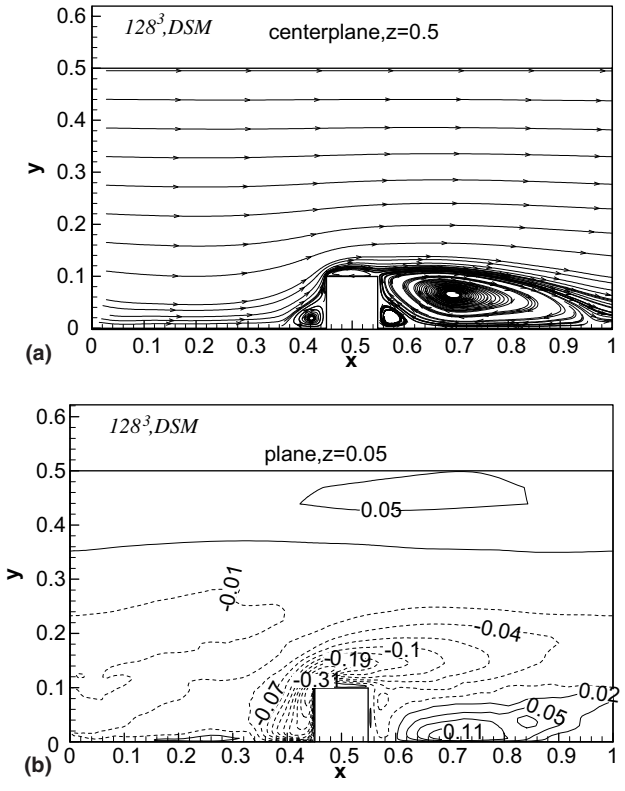

Fig. 3. (a) Mean streamline distribution in the *z*-symmetry plane. Reattachment occurs at 4.1*e* downstream of rib. The leading edge eddy extends between 0.8 and 0.9*e* upstream of rib. (b) Mean lateral or spanwise flow velocity (w_b) in the vicinity of the smooth wall. Flow impingement on the smooth wall contributes to the high Nusselt numbers in this region.

cross flow velocities (w_b) approaching 30% of the mean streamwise velocity ($\bar{u}_b$). Fig. 3(b) shows contours of w_b in a plane $z = 0.05$ in the vicinity of the smooth wall. Strong localized cross flow components are found to occur. Of particular interest is the high lateral velocity moving towards and impinging on the smooth wall within the confines of the shear layer at the leading edge of the rib. This very localized phenomenon is a result of unsteady vorticity which is produced and transported at the junction of the rib with the smooth wall. Instantaneously, the vortices draw in cooler fluid from the outside into the vicinity of the smooth wall as they are transported by the mean flow. These effects are clearly distinguishable in flow animations of coherent vorticity transport. Hence, the mean effect of these vortices is to induce a lateral flow which impinges on the smooth wall and increases the heat transfer coefficient. This "secondary flow" is much more subtle than for instance the bulk induced secondary flows that are found in angled ribs and rotating ducts, and as exemplified by the study of Ooi et al. (2002) are more difficult to predict. Ooi et al. (2002), in evaluating the prediction capability of the k–ε model, the Spalart–Allmaras model, and the v^2–f model in the same ribbed duct geometry found that all three models had difficulty in predicting the heat transfer augmentation caused by the lateral flow impingement—only the v^2–f was able to predict a qualitatively similar distribution. On the other hand, all four calculations in the present study were able to reproduce the lateral flow.

Fig. 4(a)–(e) shows contours of resolved u_{rms}, v_{rms}, w_{rms} and resolved turbulent shear stress $\overline{u'v'}$ at the center plane $z = 0.5$. The streamwise fluctuations u_{rms} are at their maximum values in the separated shear layer at the leading edge of the rib, with values between 45% and 50%. They are lowest in the stagnating flow at the rib and in the recirculation region immediately behind the rib. In the boundary layer on the ribbed wall, u_{rms} maintains a peak value between 20% and 25% over most of the ribbed surface versus 15–17% in an equilibrium boundary layer flow. Fig. 4(e) shows the distribution of u_{rms} at $x'/e = 4.5$, just downstream of reattachment. At this location the boundary layer is still recovering. Rau et al. (1998) report maximum values of 35% in the shear layer behind the ribs and 14% at the center, which compare well with 35–40% and 16%, respectively, obtained in the calculations.

The transverse fluctuations v_{rms}, at the center plane ($z = 0.5$), exhibit values of 25–27% in the stagnation region of the rib as well as in the separated shear layer downstream of the rib. The predicted values compare very well with a maximum of 24% observed by (Rau et al., 1998) in the shear layer and between 10% and 11% at the center. The cross-stream fluctuations do not exhibit a boundary layer type profile near the wall but instead increase monotonically to reach a maximum value in the separated shear layer. A typical profile is shown in Fig. 4(e).

The lateral fluctuations w_{rms}, in the symmetry plane ($z = 0.5$), exhibit a maximum value of 44% at the top leading edge of the rib. The high lateral intensities are a result of the impingement of eddies and the "splatting effect" which takes place at the leading edge of the rib. In addition to this effect, this region is home to highly unsteady eddies which form at the junction with the surface of the duct and which are sucked into the shear layer at the leading edge of the rib. The lateral fluctuations are also high in the shear layer downstream of the rib with intensities reaching 32%. At the wall boundary, peak values between 20% and 25% are maintained for most of the ribbed surface compared to 6–7% in an equilibrium boundary layer. This is shown in Fig. 4(e) for one streamwise location. It is noted that the largest anisotropies between the three normal stresses exist at the leading edge of the rib and in the near wall region, whereas the turbulence is closer to isotropy in the shear layer. In addition, of the three normal turbulent stresses, the lateral component undergoes the largest overall augmentation in the near wall region compared to a nominal boundary layer flow.

Fig. 4(d) shows the distribution of turbulent shear stress $\overline{u'v'}$ (normalized by $\bar{u}_b^2$) in the symmetry plane ($z = 0.5$). The shear stress exhibits a maximum value of -5.5% in the separated shear layer downstream of the rib. The distribution of $-\overline{u'v'}$ in the wall normal direction shown in Fig. 4(e) is completely dominated by the rib shear layer and, similar to the cross-stream fluctuations, does not show any signs of a boundary layer maximum close to the wall. This fact holds along the full extent of the ribbed wall.

Fig. 5(a)–(e) consolidates these results by showing contours of the resolved turbulent kinetic energy (*tke*) in the mid-plane for all four cases calculated. The turbulent energy is at a maximum near the origin of the shear layer on the rib with values of 21%. It decays downstream but maintains values between 10% and 13% as it approaches the next rib. In the vicinity of the ribbed wall, values between 6% and 8% are maintained throughout the length of the channel, except in the recirculation zone behind the rib in which the values are less than 5%. Thus, the presence of the rib augments *tke* by a factor of 3–4 over an equilibrium boundary layer, which exhibits a near wall maximum of 2%. At the center of the duct, the values are between 3% and 5%.

The subtle differences between the four calculations are exemplified in Fig. 5(e). The maximum value in the shear layer of 13.5% shows good agreement across all four calculations. The shear layer trajectory is predicted lower in the 128^3-DSM calculation, which results in the shorter recirculation length. However, the most important difference is the predicted level of turbulence near the ribbed wall, since it is this quantity which has

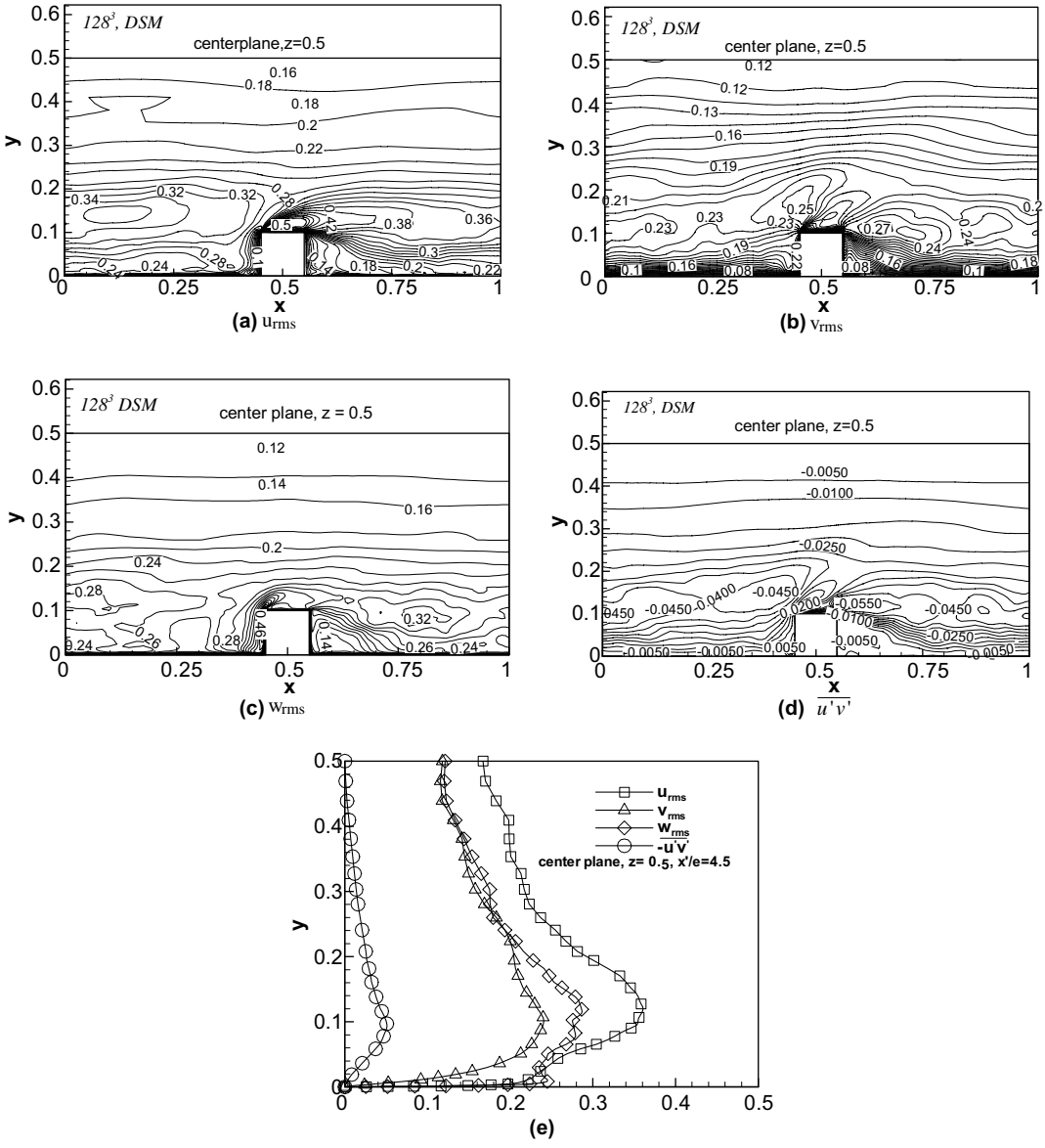

Fig. 4. Resolved turbulent quantities at center plane ($z = 0.5$). (a) u_{rms}: maximum values occur in the separated shear layer near the separation line. (b) v_{rms}: maximum values occur in the separated shear layer. The leading edge of the rib also exhibits high values. (c) w_{rms}: maximum values occur in the vicinity of the rib leading edge. (d) Distribution of turbulent shear stress. Maximum values occur in the separated shear layer and are fairly typical of free shear layers. (e) Distributions at $x'/e = 4.5$, just downstream of reattachment.

a direct impact on the prediction accuracy of the heat transfer coefficient. It is clear that the 96^3 calculation underpredicts turbulent energy in the vicinity of the ribbed wall. The dynamic subgrid stress model corrects this by the addition of turbulent viscosity, which increases the turbulent energy. This aspect of the prediction scheme plays an important role in accurately predicting the heat transfer coefficient on the ribbed surface. The increase in *tke* for the 96^3 resolution is larger than the increase in the 128^3 resolution, which is consistent with the fact that more subgrid energy is contained on the coarser mesh. This trend is also reflected consistently in the heat transfer and friction predictions summarized in Table 1.

Fig. 6 shows the Nusselt number augmentation (Nu/Nu_0) distribution for the 128^3 with DSM calculation. On the ribbed wall, the heat transfer is a maximum in front of the ribs, which is a result of the highly unsteady secondary eddies produced in this region. The vortices induce enhanced mixing and increase the heat transfer coefficient. Immediately downstream of the rib, in the recirculation region, the flow is not very energetic, as can be surmised from the turbulence intensities, and consequently there is minimal augmentation. Further

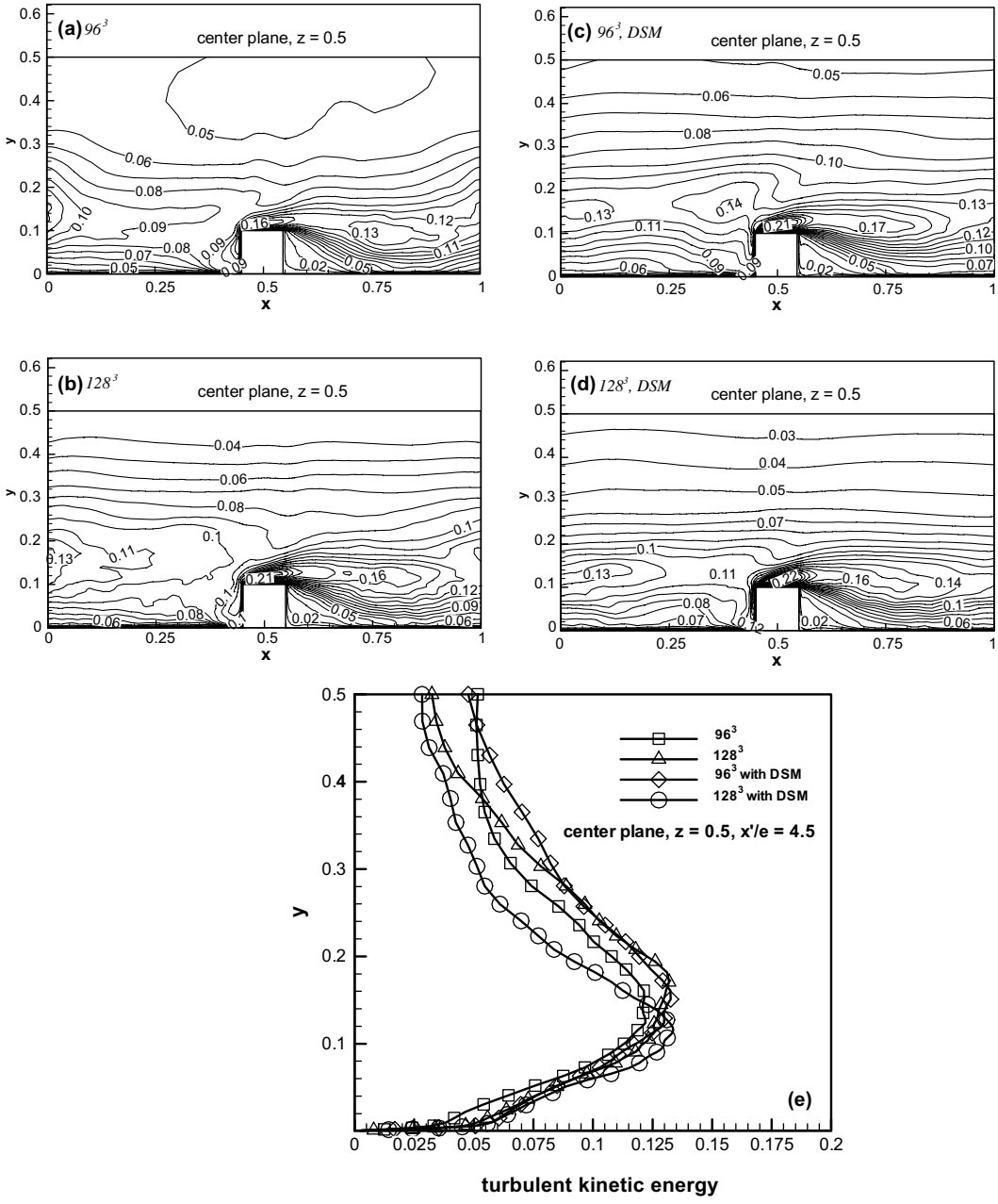

Fig. 5. Turbulent kinetic energy at center plane $z = 0.5$. (a) 96^3; (b) 128^3; (c) 96^3-DSM; (d) 128^3-DSM. Fluctuations are at a maximum in the separated shear layer. 96^3 predicts lower values of *tke* in the calculation domain, while 96^3-DSM compares well with 128^3 and 128^3-DSM. (e) Effect of mesh resolution and subgrid-scale modeling on wall normal distribution of *tke* just downstream of reattachment.

downstream, in the main recirculation zone, the augmentation increases and reaches a maximum at $x' = 3.5e$ downstream of the rib. The region of maximum heat transfer occurs where vortices from the separated shear layer "touch down" and in the mean coincides not so much with mean reattachment but rather with the region of maximum surface shear, which lies upstream of the reattachment point (Tafti, 1993). The augmentation decreases as the smooth wall is approached with values close to unity at the corners. At the smooth side wall, a region of high augmentation exists in the vicinity of the rib junction, which is a result of lateral flow impingement on the wall as shown in Fig. 3(b). On the rib itself, the heat transfer coefficient is a maximum at the top leading edge with values as high as 6 as a result of the strong fluid acceleration. Near the junction with the ribbed wall the augmentation decreases to 2.0. Although the leading edge eddies have a large effect on the floor of the duct, they do not contribute substantially to heat transfer augmentation on the

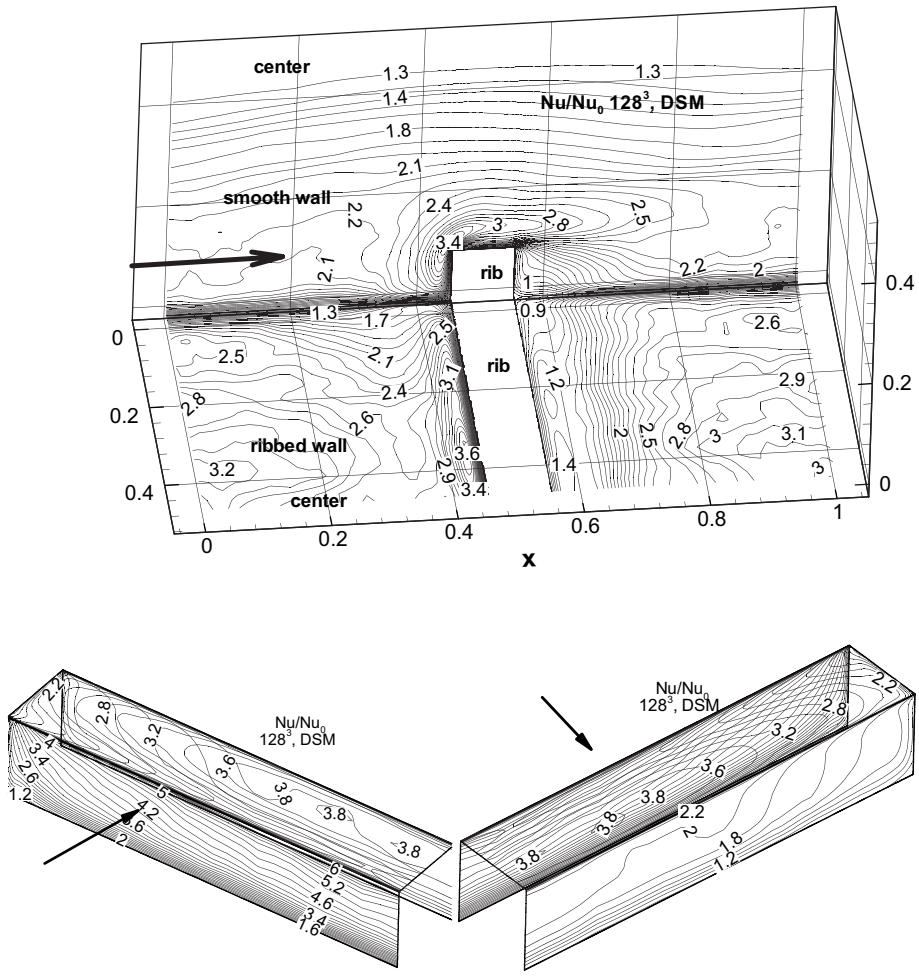

Fig. 6. Maps of Nusselt number on ribbed and smooth wall and ribs. Augmentation is at a maximum in front of the ribs, in the region near reattachment, and in the region of lateral flow impingement on the smooth wall. Ribs exhibit a maximum at the top leading edge.

rib itself. These eddies are instrumental in drawing in cooler fluid into the vicinity of the ribbed wall, but at the same time act to shield the bottom part of the rib from the freestream. On the top surface of the rib, a maximum augmentation of 3.5–3.8 is obtained, whereas on the trailing side the augmentation varies from a factor of 2 to 1.

Fig. 7(a–b) compare predicted augmentation ratios with the experiments of Rau et al. (1998) at the center of the ribbed wall ($z = 0.5$) and at a location $0.5e$ upstream of the rib along the smooth wall. In both cases the inclusion of subgrid-scale modeling gives much better prediction accuracy, whereas its exclusion causes the augmentation ratios to be underpredicted, which is consistent with observations made earlier in the paper with respect to the level of predicted turbulence. One discrepancy which still remains is the augmentation ratio at the center of the duct on the smooth wall. The predictions level to values between 1.2 and 1.4 at the center, whereas the experimental values remain much higher at 1.8. The experimental traverse does not go all the way to the center but stops at $y = 0.4$ and there is a strong possibility that the augmentation ratio will decay further towards the center of the duct. Taking that into account, the difference between computations and experiments will still exist but to a lesser extent.

The surface averaged values are tabulated in Table 1 for the ribbed and smooth walls and the rib at which the augmentation ratios are 2.4, 1.9 and 2.9, respectively. Both mesh resolutions with the dynamic model predict the overall augmentation within experimental uncertainty. The trends in the prediction accuracy of Nusselt number are consistent with previous observations. The same consistent trends are present in the friction coefficient, which is predicted to within 10% of the experimental results. In an average sense, the dynamic model calculates the correct level of turbulent viscosity for the two mesh resolutions such that the heat transfer coefficient and friction are predicted accurately, independent of the resolution, with the caveat that the resolved scales extend well into the inertial range.

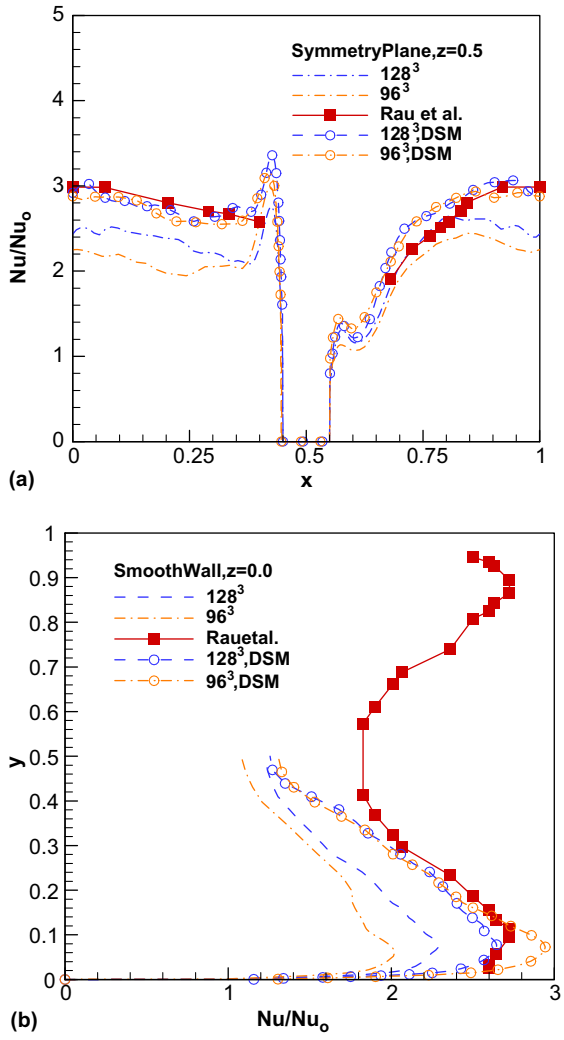

Fig. 7. Comparison with experiments of Rau et al. (1998) with $P/e = 9$ on (a) ribbed wall at center plane, $y = 0$, $z = 0.5$ (b) smooth wall at $e/2$ upstream of rib, $z = 0.0$, $x = 0.4$.

4. Conclusions

LES results are presented in a square duct with normal ribs for two mesh resolutions of 96^3 and 128^3. All calculations utilize a second-order central difference scheme. On each mesh a quasi-DNS calculation is compared to an LES calculation with the dynamic Smagorinsky subgrid scale stress model. Mean flow, turbulence, and heat transfer results are compared with the experiments of Rau et al. (1998).

All calculations reproduce the major flow structures with fidelity; namely the eddy formed at the junction between the rib and the wall, a recirculation zone formed on top of the rib and behind the rib with the corner eddy, and the lateral impingement of flow on the smooth wall. Qualitatively, the bulk flow field results are indistinguishable, but quantitative differences of 10–15% exist between the different calculations. However, there are large differences in the predicted heat transfer and friction coefficients. The degree of underprediction of heat transfer and friction varies from 20% to 30% for the 96^3 quasi-DNS calculation to 15–20% for the 128^3 quasi-DNS. This is caused primarily by low turbulence intensities. The use of LES with the dynamic model increases the level of turbulence in the flow, particularly near walls, and is able to predict the heat transfer coefficient to within experimental uncertainty and friction coefficient to within 10% of experiments for both mesh resolutions. The level of turbulence augmentation provided by the dynamic model is commensurate with the mesh resolution such that the turbulent energy, heat transfer coefficient, and friction are predicted at the right levels independent of the resolution.

Acknowledgments

The research was supported by the US DOE, Office of Fossil Energy, National Energy Technology Laboratory. Any opinions, findings, conclusions, or recommendations expressed herein are those of the author and do not necessarily reflect the views of the DOE. This work was also supported by National Computational Science Alliance under MCA98N042N and utilized the IA64 Itanium Linux cluster at the National Center for Supercomputing Applications.

References

Boris, J.P., Book, D.L., 1973. Flux-corrected transport. 1. SHASTA, a fluid transport algorithm that works. J. Comput. Phys. 11 (1), 38–69.

Boris, J.P., Grinstein, F.F., Oran, E.S., Kolbe, R.L., 1992. New insights into large eddy simulation. Fluid Dyn. Res. 10, 199–228.

Chandra, P.R., Han, J.C., Lau, S.C., 1988. Effect of rib angle on local heat/mass transfer distribution in a two-pass rib-roughened channel. ASME J. Turbomach. 110, 233–241.

Ekkad, S.V., Han, J.C., 1997. Detailed heat transfer distributions in two-pass square channels with rib turbulators. Int. J. Heat Mass Transfer 40 (11), 2525–2537.

Ferziger, J.H., 1996. Large eddy simulation, simulation and modelling of turbulent flows—Part III. In: Gatski, T.B., Hussaini, M.Y., Lumley, J.L. (Eds.), ICASE/LaRC Series in Computational Science and Engineering. Oxford University Press.

Fureby, C., Grinstein, F.F., Large eddy simulation of high Reynolds-number free & wall-bounded flows. In: AIAA 2000–2307, Fluids 2000, 19–22 June 2000, Denver, CO.

Germano, M., Piomelli, U., Moin, P., Cabot, W.H., 1991. A dynamic subgrid-scale eddy viscosity model. Phys. Fluids A 3, 1760–1765.

Han, J.C., 1984. Heat transfer and friction in channels with two opposite rib-roughened walls. ASME J. Heat Transfer 106, 774–781.

Han, J.C., 1988. Heat transfer and friction characteristics in rectangular channels with rib turbulators. ASME J. Heat Transfer 110, 321–328.

Han, J.C., Zhang, Y.M., 1991. Effect of rib-angle orientation on local mass transfer distribution in a three-pass rib-roughened channel. ASME J. Turbomach. 113, 123–130.

Han, J.C., Zhang, Y.M., Lee, C.P., 1992. Influence of surface heat flux ratio on heat transfer augmentation in square channels with parallel, crossed, and V-shaped angled ribs. ASME J. Turbomach. 114, 872–880.

Han, J.C., Al-Qahtani, M., Chen, H.C., 2002. A numerical study of flow and heat transfer in rotating rectangular channels with 45° rib turbulators by Reynolds stress turbulence model. In: Proceedings of the ASME Turbo Expo 2002, GT-2002-30216.

Incropera, F.P., Dewitt, D.P., 2002. Fundamentals of Heat and Mass Transfer, fifth ed. John Wiley and Sons, New York.

Jang, Y.J., Chen, H.C., Han, J.C., 2001. Flow and heat transfer in a rotating square channel with 45 deg. angled ribs by Reynolds stress turbulence model. ASME J. Turbomach. 123, 124–132.

Jia, R., Saidi, A., Sunden, B., 2002. Heat transfer enhancement in square ducts with V-shaped ribs of various angles. In: Proceedings of the ASME Turbo Expo, GT-2002-30209.

Korotky, G.J., Taslim, M.E., 1998. Rib heat transfer coefficient measurements in a rib-roughened square passage. ASME J. Turbomach. 120, 376–385.

Lau, S.C., McMillan, R.D., Han, J.C., 1991a. Turbulent heat transfer and friction in a square channel with discrete rib turbulators. ASME J. Turbomach. 113, 360–366.

Lau, S.C., McMillan, R.D., Han, J.C., 1991b. Heat transfer characteristics of turbulent flow in a square channel with angled discrete ribs. ASME J. Turbomach. 113, 367–374.

Lesieur, M., Metais, O., 1996. New trends in large-eddy simulations of turbulence. Ann. Rev. Fluid Mech. 28, 45–82.

Lilly, D.K., 1992. A proposed modification of the germano subgrid-scale eddy viscosity model. Phys. Fluids A 4 (3), 633–635.

Meneveau, C., Lund, T.S., Cabot, W.H., 1996. A Lagrangian dynamic subgrid-scale model of turbulence. J. Fluid Mech. 319, 353–385.

Moin, P., Squires, K., Cabot, W., Lee, S., 1991. A Dynamic sub-grid-scale model for compressible turbulence and scalar transport. Phys. Fluids A 3 (11), 2746–2757.

Murata, A., Mochizuki, S., 2001. Effect of centrifugal buoyancy on turbulent heat transfer in an orthogonally rotating square duct with transverse or angled rib turbulators. Int. J. Heat Mass Transfer 44, 2739–2750.

Murata, A., Mochizuki, S., 2000. Large eddy simulation with a dynamic subgrid-scale model of turbulent heat transfer in an orthogonally rotating rectangular duct with transverse rib turbulators. Int. J. Heat Mass Transfer 43, 1243–1259.

Najjar, F.M., Tafti, D.K., 1996. Study of discrete test filters and finite difference approximations for the dynamic subgrid-scale stress model. Phys. Fluids 8, 1076–1088.

Ooi, A., Iaccarino, G., Durbin, P.A., Behnia, M., 2002. Reynolds averaged simulation of flow and heat transfer in ribbed ducts. Int. J. Heat Fluid Flow 23, 750–757.

Prakash, C., Zerkle, R., 1992. Prediction of turbulent flow and heat transfer in a radially rotating square duct. ASME J. Turbomach. 114, 835–846.

Prakash, C., Zerkle, R., 1995. Prediction of turbulent flow and heat transfer in a ribbed rectangular duct with and without rotation. ASME J. Turbomach. 117, 255–264.

Rau, G., Cakan, M., Moeller, D., Arts, T., 1998. The Effect of periodic ribs on the local aerodynamic and heat transfer performance of a straight cooling channel. ASME J. Turbomach. 120, 368–375.

Smagorinksy, J., 1963. General circulation experiments with the primitive equations. I The basic experiment. Month. Weather Rev. 91, 99–164.

Tafti, D.K., 1993. Vorticity and scalar transport in separated and reattached flow on a blunt plate. Phys. Fluids A 5 (7), 1661–1673.

Tafti, D.K., 2001. GenIDLEST—A scalable parallel computational tool for simulating complex turbulent flows. In: Proceedings of the ASME Fluids Engineering Division, FED, ASME-IMECE, November 2001, New York, vol. 256.

Taslim, M.E., Korotky, G.J., 1998. Low-aspect ratio rib heat transfer coefficient measurements in a square channel. ASME J. Turbomach. 120, 831–838.

Taslim, M.E., Lengkong, 1998. 45 deg. staggered rib heat transfer coefficient measurements in a square channel. ASME J. Turbomach. 120, 571–580.

Taslim, M.E., Li, T., Spring, S.D., 1998. Measurements of heat transfer coefficients and friction factors in passages rib-roughened on all walls. ASME J. Turbomach. 120, 564–570.

Watanabe, K., Takahashi, T., 2002. LES simulation and experimental measurements of fully developed ribbed channel flow and heat transfer. In: Proceedings of the ASME Turbo Expo 2002, GT-2002-30203.

Zhang, Y.M., Han, J.C., Parsons, J.A., Lee, C.P., 1995. Surface heating effect on local heat transfer in a rotating two-pass square channel with 60 degree angled rib turbulators. ASME J. Turbomach. 117, 272–279.